SAE International

2012-01-0334
Published 04/16/2012

doi:10.4271/2012-01-0334
saepcelec.saejournals.org

Temperature Rise in Prismatic Polymer Lithium-Ion Batteries: An Analytic Approach

Peyman Taheri and Majid Bahrami
Simon Fraser University

ABSTRACT

A rigorous three-dimensional analytical model is proposed to investigate thermal response of batteries to transient heat generation during their operation. The modeling is based on integral-transform technique that gives a closed-form solution for the fundamental problem of heat conduction in battery cores with orthotropic thermal conductivities. The method is examined to describe spatial and temporal temperature evolution in a sample prismatic lithium-ion battery (EiG ePLB C020), subjected to transient heat generation in its bulk, and various convective cooling boundary conditions at its surfaces (the most practical case is considered, when surrounding medium is at a constant ambient temperature). The full-field solutions take the form of a rapidly converging triple infinite sum whose leading terms provide a very simple and accurate approximation of the battery thermal behavior. A surface-averaged Biot number has been proposed that can simplify the thermal solutions under certain conditions. The presented analytical model provides a fast yet accurate tool for battery thermal management system designs.

CITATION: Taheri, P. and Bahrami, M., "Temperature Rise in Prismatic Polymer Lithium-Ion Batteries: An Analytic Approach," *SAE Int. J. Passeng. Cars - Electron. Electr. Syst.* 5(1):2012, doi:10.4271/2012-01-0334.

INTRODUCTION

Among different types of rechargeable batteries, polymer lithium-ion (Li-ion) cells are well-known for their high energy and power densities (up to 150 Wh/kg), high operating voltage and discharge rate (up to about 4 V), short charging time, minimal memory effects and self-discharge (around 5% per month), and long cycling life [1]. Such desired features have made Li-ion batteries one the most favoured candidates for portable energy storage systems. More recently, the strategy of electrifying vehicles with Li-ion batteries in order to reduce or remove the contribution of internal combustion engine (ICE) into the powertrain has attracted an intense attention. Nevertheless, the persisting challenge associated with application of Li-ion batteries in hybrid-electric and plug-in electric vehicles (H/PEVs) is their temperature control. It is evident that under high discharge conditions, which involve high rates of Joulean heat generation and exothermic electrochemical reactions, batteries are prone to excessive temperature rise that can initiate swelling [2], thermal runaway [3], electrolyte fire, and in extreme cases explosion [4]. Moreover, exposure of Li-ion batteries to sub-freezing temperatures drastically reduces their energy and power [5]. As a result, design of an efficient battery thermal management system (BTMS) is crucial for batteries' safety, efficiency, and longevity.

An efficient BTMS is required to keep the batteries' temperature within a narrow range (for Li-ion batteries the ideal temperature range is 20 to 30°C), and provide a minimum temperature variation within the battery pack, i.e., a uniform temperature distribution [6]. In order to develop an effective BTMS, accurate thermal models are required to predict thermal response of the batteries under transient and dynamic load cycles [7, 8].

Thermal behavior of batteries is strongly coupled to the electro-chemical processes during charge and discharge cycles [9, 10]. However, for large-scale battery assemblies, e.g., in hybrid and electric vehicles, the collective thermal effects of electro-chemical processes can be approximated from measurements, and then considered as the heat source in a standalone thermal model. Based on this decoupling strategy, there are several battery thermal models available in the literature including one-dimensional [11], two-dimensional [12, 13, 14], and three-dimensional models [15, 16, 17, 18], in which variety of cell designs, modes of operation, and thermophysical properties are considered. For an extensive bibliography on battery thermal models see Ref. [10].

Advanced simulations for Li-ion batteries suggest that owing to their laminated structure, a three-dimensional thermal analysis should be adapted to properly study thermal

response of the batteries during cyclic operation. To the author's best knowledge, all the multidimensional thermal models developed for Li-ion batteries rely on numerical solution; thus, lack of a theoretical method is evident. The only available analytical solution is the work of Newman and Tiedemann [19], where the classical technique of separation of variables is employed to solve the transient heat conduction problem for batteries with a constant heat generation and constant-temperature boundary conditions. In this study, we investigate the same problem featuring transient heat generation and convective boundary conditions that yield a more realistic representation of the operating conditions for Li-ion batteries used in applications such as H/PEVs. In our approach, since both energy equation and boundary conditions involve non-homogeneities, the integral-transform technique [20, 21] is used to obtain a closed form analytical solution.

In the following sections, the analytical thermal model is presented, and its application for a sample polymer Li-ion battery is demonstrated. Thermal behavior of the battery is investigated during galvanostatic discharge processes with different discharge currents, while convective cooling is applied at its surfaces. Heat generation rates within the battery are approximated from voltage drop measurements at constant discharge currents, available from battery manufacturer. Finally, the required convective heat transfer coefficients which must be provided by the BTMS are discussed.

THERMAL MODEL FORMULATION

We consider a three-dimensional rectangular orthotropic solid of length L_1, width L_2, and height L_3. Heat in generated within the solid domain, while heat transfer with surrounding medium is allowed at its boundary surfaces. The temperature distribution inside the solid is described by energy balance equation that only includes conduction terms,

$$\rho c_p \frac{\partial T}{\partial t} = k_1 \frac{\partial^2 T}{\partial x_1^2} + k_2 \frac{\partial^2 T}{\partial x_2^2} + k_3 \frac{\partial^2 T}{\partial x_3^2} + g \quad \text{in}$$

$$0 \le x_1 \le L_1, \quad 0 \le x_2 \le L_2, \quad 0 \le x_3 \le L_3$$

(1)

in which, t is time and $\mathbf{x} = (x_1, x_2, x_3)$ represent the components of position vector in Cartesian coordinate system. The density ρ, heat capacity per unit mass c_p, and orthotropic thermal conductivity coefficients (k_1, k_2, k_3) are the thermophysical parameters. The functions $T(\mathbf{x}, t)$ and $g(\mathbf{x}, t)$ represent the temperature filed and heat generation rate per unit volume, respectively. It should be noted that in derivation of Eq. (1), the thermophysical properties are assumed to be independent of temperature, which is generally acceptable over a reasonably narrow temperature range of interest, i.e., the desired operating temperature range. This is a key assumption which leads to a linear energy balance equation [cf. Eq. (1)] and allows an analytical solution.

At the boundaries of the domain convective heat transfer is considered,

$$-k_i \frac{\partial T}{\partial x_i} + h_{i0}\left(T - T_0\right) = 0 \quad \text{at} \quad x_i = 0 \ \ (i = 1,2,3)$$

(2-1)

$$k_i \frac{\partial T}{\partial x_i} + h_{i1}\left(T - T_0\right) = 0 \quad \text{at} \quad x_i = L_i \ \ (i = 1,2,3)$$

(2-2)

where T_0 is the ambient temperature, also the initial temperature of the domain (battery),

$$T = T_0 \quad \text{at} \quad t = 0$$

(3)

In this study, we consider constant ambient temperatures; however, the method allows definition of ambient temperatures as a function of both space and time [20, 21, 22]. At x_i-direction, the convective heat transfer coefficients on surface 0 (the surface at $x_i = 0$) and surface 1 (the surface $x_i = L_i$) are denoted by h_{i0} and h_{i1} (i =1,2,3).

The system of initial boundary value problem, described in Eqs. (1), (2), (3), can be transformed into a more convenient form

$$\frac{\partial \theta}{\partial \tau} = \frac{\partial^2 \theta}{\partial X_1^2} + K_2 \frac{\partial^2 \theta}{\partial X_2^2} + K_3 \frac{\partial^2 \theta}{\partial X_3^2} + G \quad \text{in}$$

$$0 \le X_1 \le 1, \quad 0 \le X_2 \le 1, \quad 0 \le X_3 \le 1$$

(4)

with boundary conditions,

$$-\frac{\partial \theta}{\partial X_i} + \mathrm{Bi}_{i0}\theta = 0 \quad \text{at} \quad X_i = 0 \ \ (i = 1,2,3)$$

(5-1)

$$\frac{\partial \theta}{\partial X_i} + \mathrm{Bi}_{i1}\theta = 0 \quad \text{at} \quad X_i = 1 \ \ (i = 1,2,3)$$

(5-2)

and the initial condition

$$\theta = 0 \quad \text{at} \quad \tau = 0$$

(6)

In the transformed system, the dimensionless space and time are defined as,

$$X_i = \frac{x_i}{L_i} \ \ (i = 1,2,3), \quad \tau = \frac{k_1 / L_1^2}{\rho c_p / t}$$

(7-1)

and

$$K_i = \frac{k_i / L_i^2}{k_1 / L_1^2} \ (i = 1,2,3), \quad \mathrm{Bi}_{ij} = \frac{h_{ij} L_i}{k_i} \ (i = 1,2,3;\ j = 0,1) \tag{7-2}$$

where Bi_{ij} are the Biot numbers. The temperature rise θ, and the source for temperature rise G in temperature unit are

$$\theta = T - T_0, \quad \text{and} \quad G = \frac{g}{k_1 / L_1^2} \tag{7-3}$$

The transformed system (4), (5), (6), which describes the temperature rise with respect to dimensionless space and time, is solved by applying a finite-integral transform technique [20, 21], as described in the Appendix.

STRUCTURE AND THERMOPHYSICAL PROPERTIES OF THE SAMPLE POLYMER LITHIUM-ION BATTERY

Prismatic polymer Li-ion batteries use specific battery architecture; the liquid lithium-salt electrolyte is held within the multi-layered porous structures of electrodes and separator sheets, which are made of solid polymer composites. Application of porous electrodes promotes intimate contact of the electrode material with the electrolyte solution, leading to higher rate of chemical reactions. Figure 1(a) schematically shows the internal multi-layered structure of a prismatic polymer Li-ion battery, in which negative and positive porous electrodes are alternatively wrapped in separator sheets. A battery core as shown in Fig. 1(b), includes several layers of electrodes and separators enclosed in a case (the case is not shown). A unit cell of the battery layered arrangement is depicted in Fig. 1(c), in which lithium ions Li^+ are migrating from anode to cathode during a discharge process.

In order to demonstrate how to apply the proposed thermal model for batteries, ePLB C020 battery fabricated by EiG Corporation (South Korea) is considered as our sample Li-ion battery. This battery uses $Li[NiCoMn_2]O_2$ and graphite as active materials at cathode and anode, respectively. The nominal voltage and capacity the battery are 3.65 V and 20 Ah, with specific energy of 175 $Wh \cdot kg^{-1}$. The weight of the battery is approximately 407 g, thus, its energy content is approximately 71 Wh. Mechanical and electrical specifications of the battery are listed in Table 1.

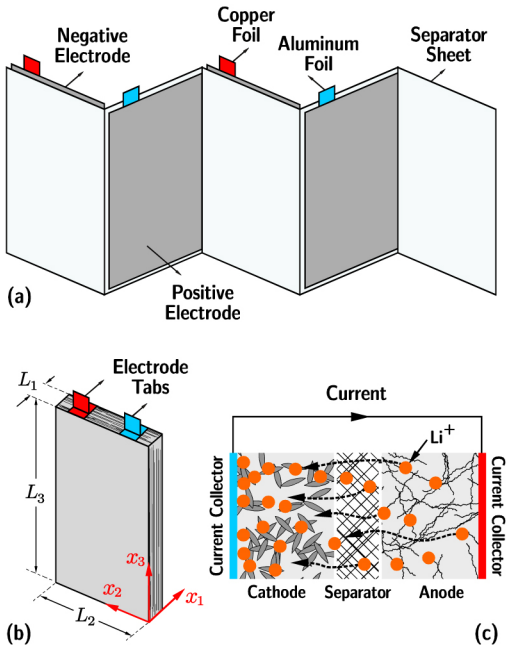

Figure 1. (a) Multi-layered core configuration in a prismatic polymer lithium-ion battery; (b) Core of a single battery pack (the battery case is not shown); (c) A unit cell of the battery including a pair of porous electrodes, a porous separator, and current collectors is shown during discharge process. The pores of polymer components, i.e., electrodes and separator are filled with an electrolyte liquid which allows migration of ions between the electrodes.

The sample battery includes 18 layers of negative electrodes, 17 layers of positive electrodes, and 36 layers of polymer (polypropylene) separator sheets. The electrodes which include current collector foils laminated by thin layers of a polymer (polyethylene oxide) are connected in parallel. Aluminum and copper foils are used as current collectors in positive and negative electrodes, respectively. The polymer layers (electrodes and separator sheets) are porous media soaked in an electrolyte liquid (a mixture of Ethylene carbonate and Dimethyl carbonate) and accommodate active materials required in the battery chemistry. The battery core [Fig. 1(a)] is packed in a polymer laminate aluminum pouch case. The thickness and thermophysical properties of the battery core layers/materials are provided in Table 2. Density, heat capacity, and thermal conductivity of porous polymer layers in the electrodes and separator sheets must be measured after they are soaked in the electrolyte liquid. Since heat capacity and thermal conductivity of wet layers are not reported by the manufacturer, thus we use available data in the literature for a similar battery type [14, 18].

Table 1. Specifications of ePLB C020, EiG battery.

Mechanical characteristics	
Thickness (L_1)	7 [mm]
Width (L_2)	125 [mm]
Height (L_3)	195 [mm]
Weight	407 [g]
Electrical characteristics	
Nominal voltage	3.65 [V]
Nominal capacity	20 [Ah]
Specific energy	175 [Wh kg^{-1}]
Energy density	370 [Wh L^{-1}]
Specific power (DOD 50%, 10 sec.)	2300 [W kg^{-1}]
Power density (DOD 50%, 10 sec.)	4600 [W L^{-1}]
Operating conditions	
Recommended voltage limit for discharge	3 [V]
Lower voltage limit for discharge	2.5 [V]
Maximum continuous discharge current	5*C*
Maximum discharge current (peak < 10 second)	10*C*
Operating temperature	between -30°C and +50°C
Recommended charge temperature	between 0°C and +40°C

Table 2. Thickness and thermophysical properties of battery components.

Material/Layer	Thickness [μm]	Number of layers	Density [$kg \cdot m^{-3}$]	Heat capacity [$J \cdot kg^{-1} \cdot K^{-1}$]	Thermal Conductivity [$W \cdot m^{-1} \cdot K^{-1}$]
Aluminum foil	21	17	2702	903	238
Copper foil	12	18	8933	385	398
Separator sheet	25	36	1017 (wet)	1978 (wet)	0.34 (wet)
Positive electrode	70	34	2895 (wet)	1270 (wet)	1.58 (wet)
Negative electrode	79	36	1555 (wet)	1437 (wet)	1.04 (wet)

In order to solve Eqs. (1), (2), (3), it is necessary to determine the thermophysical parameters for the battery core. To avoid complexities associated with its multi-material multi-layered structure, we define average/effective transport properties. The product value of density and heat capacity are approximated based on the volume of each layer (component) [10, 18],

$$\rho c_p = \frac{\sum_{j=1}^{N} \rho_j c_{p,j} \mathcal{V}_j}{\mathcal{V}} \qquad (8)$$

where $\mathcal{V}$ is the total battery volume, $\mathcal{V}_j$ is the volume of the *j*th component (layer), and *N* is the total number of components (layers). Furthermore, the concept of "equivalent resistance network" is employed to define effective thermal conductivities in different directions. Based on Fig. 1, there are series thermal resistors in x_1-direction and parallel thermal resistors in x_2- and x_3-directions. Accordingly, through-plane and in-plane orthotropic conductivities are obtained as [8, 10],

$$k_1 = \frac{\sum_{j=1}^{N} \ell_j}{\sum_{j=1}^{N} \left(\ell_j / k_j \right)} \quad \text{and} \quad k_2 = k_3 = \frac{\sum_{j=1}^{N} \ell_j k_j}{\sum_{j=1}^{N} \ell_j} \qquad (9)$$

where ℓ_j denotes the thickness of the *j* th component (layer) in x_1-direction, and $\sum_{j=1}^{N} \ell_j = L_1$. It must be emphasized that as a consequence of laminated arrangement of the battery core, interfacial phenomena of contact resistance at porous-porous and porous-solid interfaces must be considered in evaluation of effective thermal conductivities. However, for polymer Li-ion batteries, since the contact interfaces are wet at the presence of the electrolyte liquid, the effects of contact resistance are assumed to be negligible. This simplification is usually justified with the fact that thermal conductivities of electrolyte and polymer compounds are in the same order. Detailed experimental study on contact resistance issue in batteries is not available, and the authors believe that this important phenomenon is overlooked and plan to further investigate this potentially critical issue in depth.

The pouch case of the battery is made of polyethylene-laminated aluminum foil. Due to its small thickness (162 μm) and polyethylene laminates, the heat capacity and thermal conductivity of the case is negligible, hence, its effects can be excluded from the thermal analysis.

To complete our definition of the initial boundary value problem (1), (2), (3), heat generation rate $g(\mathbf{x}, t)$ should be determined. One of the most challenging tasks in thermal modeling of batteries is the evaluation of heat generation rate during their operation. Complexities associated with this task are rooted in the strong coupling of heat generation rate to chemical reactions rates, and Joule heating inside the battery structure [9]. In this study, first we consider homogeneous heat generation rates inside the battery, i.e., $g = g(t)$, approximated from Bernardi's equation [23]. Furthermore, capability of the proposed method to take account for non-homogeneous heat generation rates is demonstrated in the next section. The fact should be highlighted that in reality, heat generation is non-homogeneous due to current density distribution and local internal resistance [14]. Accordingly, to accommodate the actual non-homogeneous heat generation in the present model, it must be coupled to an electrical model.

Bernardi *et al.* [23] proposed a general energy balance equation for battery thermal models in which the homogeneous heat generation rate is given by

$$g = \frac{I}{\mathcal{V}}\left[\left(V_{oc} - V\right) - T\frac{\mathrm{d}V_{oc}}{\mathrm{d}T}\right] \qquad (10)$$

The above equation is accurate enough to perform detailed thermal analysis at single battery and module levels [18]. The parameters I and V denote operational current ($I > 0$ for discharging and $I < 0$ for charging) and voltage of the battery, and $\mathcal{V}$ is the battery volume. Open circuit potential (OCP) of the battery is denoted by V_{oc}. The term $I\,(V_{oc} - V)$ is the irreversible heat due to cell overpotential (electrodes polarization), and $IT\,(\mathrm{d}V_{oc} / \mathrm{d}T)$ is the reversible heat caused by the entropy change of electrochemical reactions [23, 24]. For Li-ion batteries, during normal operational temperatures, the derivative $\mathrm{d}V_{oc} / \mathrm{d}T$ is a very small constant [18] and can be safely neglected. To justify this assumption, it suffices to mention that OCP in Li-ion batteries, which is measured in non-operating condition, is a strong function of ion concentration, and not the temperature. Nonetheless, at very high and low temperatures the dependency of OCP on temperature is considerable [25].

Experimental data, reported by EiG for its ePLB C020 cell, on variation of cell potential (voltage) versus depth-of-discharge (DOD) for different discharge rates are shown in Fig 2. For discharge processes, the cut-off voltage of 3 V is considered. In the proceeding section these discharge data along with Eq. (10) are used to approximate the heat generation rate inside the battery.

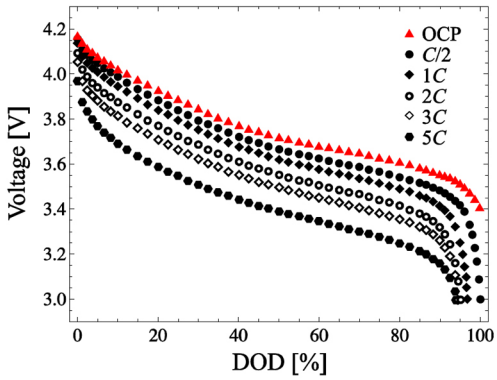

Figure 2. Experimental data (reported by EiG Corp.) on variation of battery voltage versus depth-of-discharge (DOD or utilization) for different discharge conditions in C-rate. A 1C-rate means that the discharge current will discharge the entire battery in 1 hour. The triangle symbols represent open circuit potential (OCP).

RESULTS AND DISCUSSION

In this section, thermal behavior of the sample Li-ion battery during discharge processes is investigated using the proposed analytical approach. The computational procedure as presented in the Appendix, are programmed symbolically in Mathematica® to obtain a generic solution in series form, i.e., Eq. (A-10). It should be noted that compared to existing multi-dimensional numerical approaches, e.g., [11, 12, 13, 14, 15, 16, 17, 18], our analytical method is very fast, since it requires minimum numerical effort; please see the Appendix.

The dimensions of the battery as given in Table 1 are chosen to be $L_1 = 0.007$ m, $L_2 = 0.125$ m, and $L_3 = 0.195$ m. The effective thermophysical properties of the battery core are evaluated from Eqs. (8) and (9), for which the required data are provided in Tables 1 and 2. The values for thermophysical properties of the sample battery are estimated

$$\rho c_p = 2767.45\ \frac{\mathrm{kJ}}{\mathrm{m^3\ K}},$$
$$k_1 = 0.97\ \frac{\mathrm{W}}{\mathrm{m\ K}},\quad k_2 = k_3 = 26.57\ \frac{\mathrm{W}}{\mathrm{m\ K}} \qquad (11)$$

Since the capacity of the sample battery is 20 Ah, the empirical data for $C/2$, $1C$, $2C$, $3C$, and $5C$ discharge rates conditions, as shown in Fig. 2, correspond to 10 A, 20 A, 40 A, 60 A, and 100 A discharge currents, during 2 hours, 1 hour, 30 minutes, 20 minutes, and 12 minutes, respectively. For different discharge modes, homogeneous heat generation rates $g(t)$, are obtained by fitting high-order polynomials to the data points in Fig. 2, and using Eqs. (10) and (7-3) while assuming $\mathrm{d}V_{oc} / \mathrm{d}T \approx 0$. Curves in Fig. 3 show the variation of volumetric heat generation rates versus DOD during galvanostatic discharge processes. The sharp increase of g at

the end of discharge is rooted in the large differences between OCP and operating voltages.

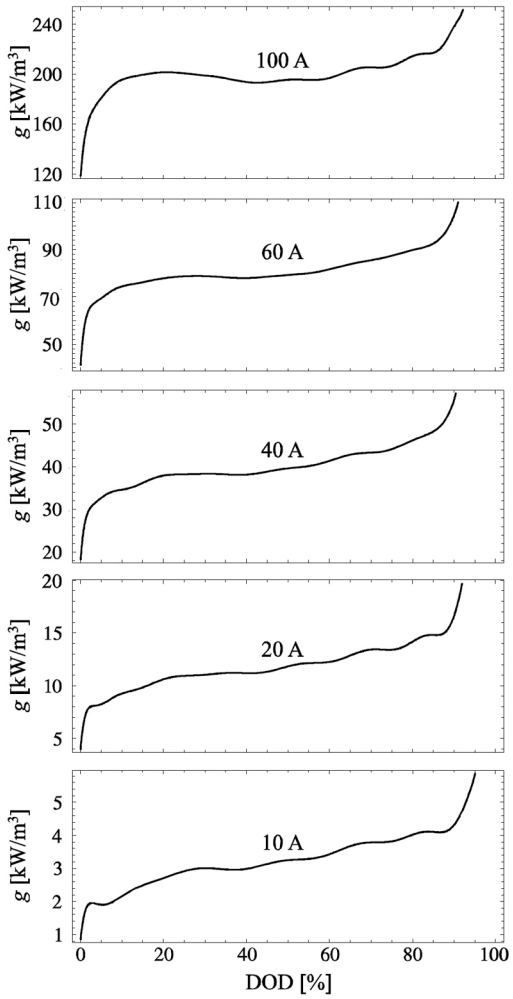

Figure 3. Variation of heat generation rate versus depth of discharge for ePLB C020 battery at different discharge currents.

Battery thermal management systems operate based on heat transfer at battery surfaces, and their design depends on a variety of parameters, including: i) cooling strategy, that can be either active or passive [26] or a combination; ii) the type of the coolant; iii) coolant circulation design; iv) the size and the shape of the battery assembly; v) recommended operational temperature for the battery, to name a few. We assume small and moderate heat transfer coefficients $h_{ij} < 20$, to investigate the possibility of natural and forced convection cooling with air. Also, constant heat transfer coefficients h_{ij} at all surfaces are considered, albeit the method can handle different values for heat transfer coefficients, as will be shown later in this section. The ambient and initial temperatures are assumed to be T_0 = 20°C (293 K), thus, based on the recommended operation temperature in Table 1, the maximum temperature rise of θ = 30°C is acceptable during the battery operation. Here, only discharge operation mode is considered, but the same method can be applied for charging process if variations of OCP and operation voltage are given during charging period.

In Figs. 4, 5, 6, maximum temperature rise θ_{Max} at the center of the battery **X** = (0.5,0.5,0.5), and minimum temperature rise θ_{Min} at the corners of the battery, e.g., **X** = (0,0,0), are plotted and compared to an average temperature rise θ_{Ave} which is defined as

$$\theta_{Ave} = \int_0^1 \int_0^1 \int_0^1 \theta(X_1, X_2, X_3, \tau) \cdot \mathrm{d}X_3 \cdot \mathrm{d}X_2 \cdot \mathrm{d}X_1 \qquad (12)$$

In Fig. 4, the maximum, minimum, and average temperature rise during 10 A and 20 A discharge are plotted for convective heat transfer coefficients of h = {0, 5, 10, 20} $\mathrm{W \cdot m^{-2} \cdot k^{-1}}$. At the end of the discharge processes the temperature rise in the adiabatic battery (h = 0) is about 9 K for 10 A, and 16 K for 20 A discharge processes (not shown in the plots). The results show that cooling effect of natural convection (h = 5 $\mathrm{W \cdot m^{-2} \cdot k^{-1}}$) is significant only when the rate of heat generation is low. As the rate of heat generation increases the temperature difference between adiabatic and natural convection conditions decreases; compare Fig. 4(a) and (b).

In Fig. 5, temperature rise corresponding to discharge currents of 40 A, 60 A and 100 A are shown. To keep the temperature rise within the allowed range (less than 30 K), a relatively low convective heat transfer (e.g., natural convection) with h = 5 $\mathrm{W \cdot m^{-2} \cdot k^{-1}}$ suffices for the 40 A discharge case; however, for more rigorous discharge situations, e.g., 100 A, forced convection cooling (or liquid coolant) providing h > 20 $\mathrm{W \cdot m^{-2} \cdot k^{-1}}$ is necessary. We remind that a battery initial temperature of T_0 = 20°C has been assumed here; in real application and under heavy duty cycles, the results and cooling requirements will vary. Since sudden temperature rise are expected at the end of discharging, it is recommended to utilize the battery up to 90% DOD, equivalent to 10% state-of-charge (SOC). Also note that higher rates of heat generation and surface heat dissipation yield strong temperature non-uniformities in the battery, i.e., the difference between min. and max. temperatures increases.

Throughout the results, the average temperature θ_{Ave} is closer to the maximum temperature rather than the minimum temperature. This trend is more visible in Fig. 5(c), which indicates only a small portion of the battery has temperatures close to the minimum temperature region, which occurs at the corners, due to low thermal conductivity of the battery bulk (see Fig. 6).

When θ_{Max}-θ_{Min} is small, one can use a lumped thermal model to approximate the thermal behavior of the battery. Conventionally, Biot number is used to indicate the applicability of lumped thermal models; a Biot number less

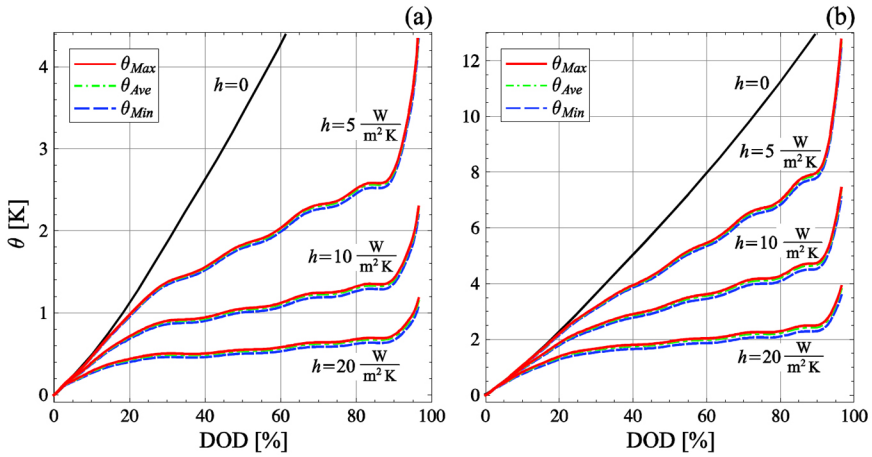

Figure 4. Temperature rise in the battery during 10 A discharge (plot a) and 20 A discharge (plot b) are shown for h = {0, 5, 10, 20} W·m^{-2}·K^{-1}. Maximum temperature rise at the battery center (red solid-line) and minimum temperature rise at the battery corners (blue dashed-line), are compared to average temperature (green dot dashed-line). The solid black line corresponds to adiabatic temperature rise (h = 0).

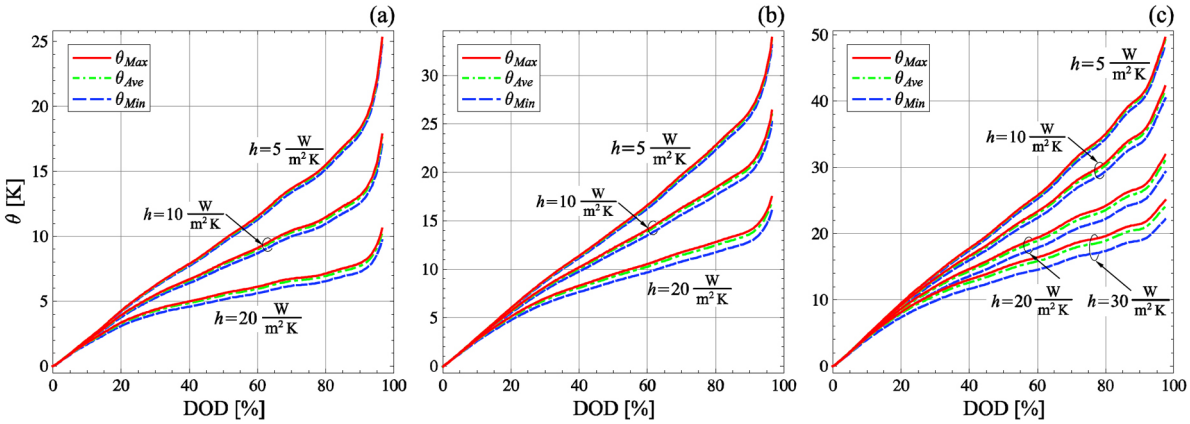

Figure 5. For different convective heat transfer coefficients at the battery surface, temperature rise within the battery for discharge rates of 40 A (plot a), 60 A (plot b), and 100 A (plot c) are shown. The maximum temperature rise at the battery center (red solid-line) and the minimum temperature rise at the battery corners (blue dashed-line), are compared to the average temperature rise (green dot dashed-line).

than 0.1 typically indicates a less than 5% error due to the lumped model assumption [27].

We define a surface-averaged Biot numbers for the battery

$$\mathrm{Bi}_{Ave} = \frac{1}{A}\sum_{i=1}^{3}\sum_{j=1}^{2}\mathrm{Bi}_{ij}A_{ij} = \frac{L_1L_2L_3}{k_1k_2k_3}\left(\frac{k_1k_2h_{3j}+k_1k_3h_{2j}+k_2k_3h_{1j}}{L_1L_2+L_1L_3+L_2L_3}\right)\ (j=1\text{or }2) \qquad (13)$$

where A is the total battery surface area, and A_{ij} is the area of the surface normal to x_i-direction; $j = 0$ and $j = 1$ denote the surface at $x_i = 0$ and $x_i = L_i$, respectively. Biot number Bi_{ij} characterizes the ratio of convective heat transfer to conduction heat transfer at A_{ij} surfaces. Since thermal conductivity and dimensions of the battery are invariant, the only parameter affecting Bi_{ij} is h_{ij}. In Table 3, Biot numbers for some cases are listed. The surface-averaged Biot number suggests that for $h < 15$ W·m^{-2}·k^{-1} at all surfaces, a lumped thermal model is acceptable since $\mathrm{Bi}_{Ave} < 0.1$. For forced-convective cases with $h > 15$ W·m^{-2}·k^{-1} a multi-dimensional approach must be applied as $\mathrm{Bi}_{Ave} > 0.1$; however, since Biot number in x_2-direction is always less than the other two directions (see Table 3), a two-dimensional model in x_1-x_3 plane is also acceptable. Note that increasing of h in x_2-direction can change the choice for a two-dimensional model.

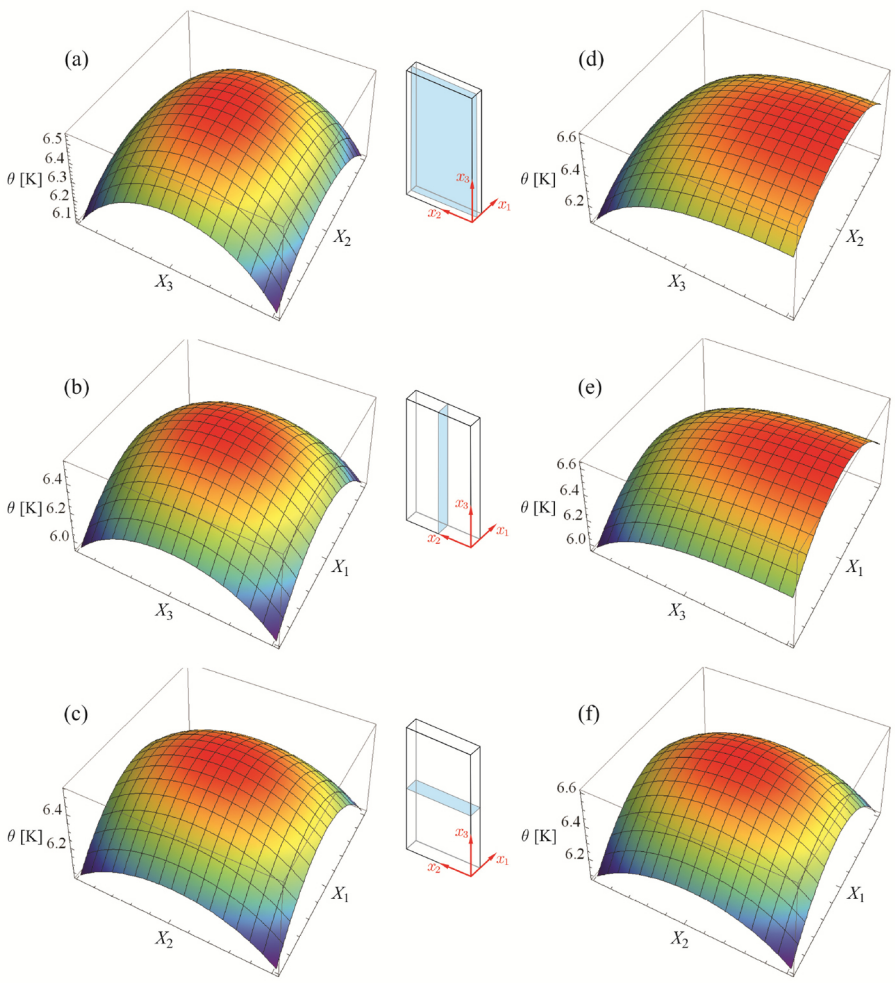

Figure 6. Plots (a)-(c): Temperature (rise) distribution at the end of 40 A discharge process is shown for h_{ij} = 30 W·m^{-2}·K^{-1} at all surfaces of the battery. Plots (d)-(f): Temperature (rise) distribution at the end of 40 A discharge process is shown for h_{31} = 2 W·m^{-2}·K^{-1} and h_{ij} = 30 W·m^{-2}·K^{-1} for other surfaces. Ambient and initial temperature of 293 K was assumed. As a result of the system transformation, the results are mapped into a square region.

Table 3. Directional and surface-averaged Biot numbers.

Heat transfer coefficient [W·m^{-2}·K^{-1}]	Bi_{1j}	Bi_{2j}	Bi_{3j}	Bi_{Ave}
h = 5	0.036	0.023	0.037	0.035
h = 10	0.072	0.047	0.073	0.071
h = 15	0.108	0.070	0.110	0.106
h = 20	0.144	0.094	0.147	0.141
h = 30	0.216	0.141	0.220	0.213

In Fig. 6, temperature rise at the end of a 40 A discharge process is shown on X_1 = 1/2, X_2 = 1/2, and X_3 = 1/2 planes. Plots (a)-(c) show the temperature rise when h_{ij}=30 W·m^{-2} · k^{-1} is applied on all boundaries. Plots (d)-(f) correspond to the case in which h_{31} = 2 W·m^{-2}·k^{-1}, and on other surfaces h_{ij} = 30 W·m^{-2}·k^{-1}. The latter case is defined to examine the effects of non-uniform boundary conditions on the temperature distribution. In practical applications, indeed, at one side of the battery that is used for electrical connections, heat transfer coefficient differs from the other sides (usually less); this alters the pattern of temperature distribution.

Plots (a)-(c) in Fig. 6 have the maximum temperature rise of θ_{Max} = 6.47 K, whereas the minimum temperature rise exists at the corners of X_1-X_3 plane. This confirms the result of Biot number analysis, i.e., the best geometry choice for a two-dimensional modeling is a x_1-x_3 surface. This argument applies also for plots (d)-(f).

As a result of system transformation, i.e., Eq. (7), the solutions are mapped into a square region. A simple backward transformation can be used to remap the solutions into the original physical dimensions.

The experimental observations in [14] show that maximum temperature in pouch batteries exists in the vicinity of their terminal tabs, where current density is maximum. Since our thermal model is not coupled with an electrical model, we examine the effects of non-homogeneous heat generation by defining,

$$G_n\left(X_3,\tau\right)=G_J(X_3)+G(\tau) \tag{14}$$

where $G_J(X_3)$ is assumed as an arbitrary source for temperature rise due to Joulean heat generation, and $G(\tau)$ is the homogeneous source of temperature rise defined by Eqs. (10) and (7-3). Consequently, $G_n(X_3, \tau)$ represents a non-homogeneous heat source. Here, for simplicity we consider Joule heating as a function of X_3 only,

$$G_J(X_3)=\mathrm{Sin}\left(\frac{X_3}{3}\right)\quad(0\le X_3\le 1) \tag{15}$$

In Fig. 7, temperature (rise) distribution at the end of a 40 A discharge process with the above non-homogeneous heat generation rate is shown on $X_1 = 1/2$, $X_2 = 1/2$, and $X_3 = 1/2$ planes. Boundary conditions at all surfaces are the same with h_{ij} = 30 $\mathrm{W{\cdot}m^{-2}{\cdot}k^{-1}}$. As $X_3 \rightarrow 1$, the magnitude of joule heating increases, and in contrast to the case of homogeneous heat generation, location of θ_{Max} is not at the battery center.

In order to find a cut-off limit for the infinite summation in series solution (A-2), steady-state errors for problems with constant heat generation were calculated. Based on our investigation, if eigenvalues are evaluated accurately (rounded to 16 significant digits), 12 eigenvalues in each direction will suffice to achieve temperature rise solutions with less than 1% error. Finally, we examined the correctness of the computational procedure by applying a very small heat transfer coefficient. As expected, when $h_{ij} \rightarrow 0$, the solution converged to adiabatic solution which can be determined by integrating the following equation over the discharge time

$$\frac{\mathrm{d}\theta}{\mathrm{d}\tau}=G\left(\tau\right) \tag{16}$$

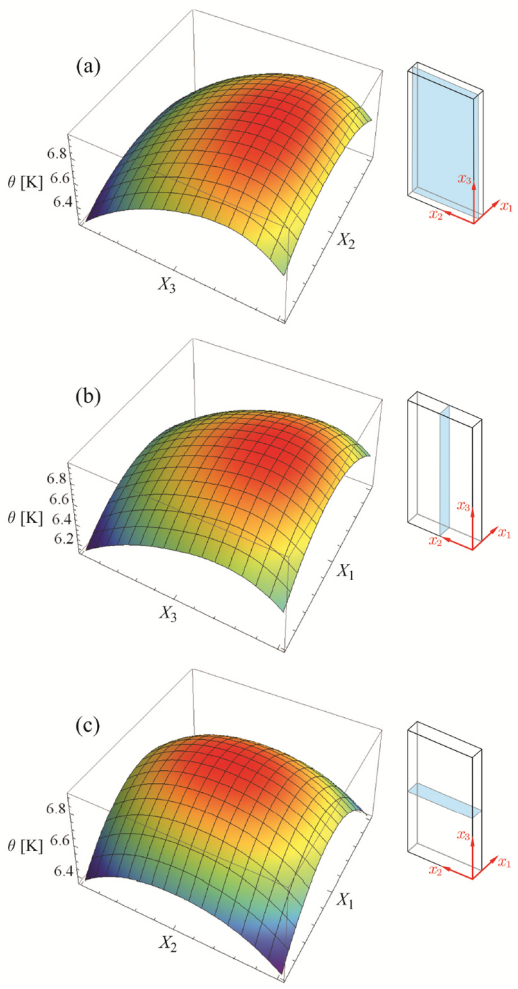

Figure 7. Temperature (rise) distribution at the end of 40 A discharge process with non-homogeneous heat generation rate is shown for h_{ij} = 30 $W{\cdot}m^{-2}{\cdot}K^{-1}$ at all surfaces of the battery. Ambient and initial temperature of 293 K was assumed. As a result of the system transformation, the results are mapped into a square region.

CONCLUSION

Based on the classical integral-transform technique, a closed form solution was developed to evaluate temperature rise in polymer Li-ion batteries. The proposed approach takes account for: i) multi-dimensional heat diffusion, ii) orthotropic thermal conductivities, iii) transient heat generation rate, and iv) convective boundary condition, and provide a useful and reliable tool for investigating thermal behavior of batteries under various conditions.

The proposed analytical model was employed to study the temperature rise in a single prismatic Li-ion battery (ePLB C020, EiG Corp., South Korea) during discharge processes, where transient heat generation rate was approximated from

the electrical performance of the battery. The obtained results showed that for the single battery cell, natural convection with heat transfer coefficients $h < 5$ W·m^{-2}·k^{-1} can prevent battery overheating during discharge processes with $I < 40$ A, when a room temperature was considered as the initial battery temperature. For more aggressive discharge conditions higher heat transfer rates at battery surface are required, e.g., forced-convection.

In large battery assemblies the issue of temperature rise becomes more critical, as heat accumulates at the center of the battery module. Indeed, adaptation of the proposed method to battery modules is a straightforward task, for which other practical and engineering consideration such as thermal contact resistances between different components of the assembly, i.e., battery cells and module case, should be considered. Furthermore, the presented procedure can be used to investigate thermal behavior of Li-ion batteries during cyclic loads.

CONTACT INFORMATION

Peyman Taheri
Laboratory for Alternative Energy Conversion (LAEC)
Mechatronic Systems Engineering, School of Engineering Science
Simon Fraser University, Surrey, BC V3T 0A3, Canada
ptaherib@sfu.ca
Fax: +1 (778) 782-7514

Majid Bahrami
Associate Professor, Mechatronic Systems Engineering, School of Engineering Science
Simon Fraser University, Surrey, BC V3T 0A3, Canada
mbahrami@sfu.ca

ACKNOWLEDGEMETS

This work was supported by Automotive Partnership Canada (APC), Grant No. APCPJ 401826-10. The authors would like to thank the support of the industry partner of the project, Future Vehicle Technologies Inc. (Maple Ridge, British Columbia, Canada).

REFERENCES

1. Hossain, S., in *Handbook of batteries*, 2nd ed., Linden, D., Editor, p. 36.1, McGraw-Hill, New York (1995).
2. Lee, K.H., Song, E.H., Lee, J.Y., Jung, B.H., and Lim, H.S., "Mechanism of gas build-up in a Li-ion cell at elevated temperature," *J. Power Sources*, Vol. 132, pp. 201-205 (2004).
3. Mandal, B.K. et. al, "Thermal runaway inhibitors for lithium battery electrolytes," *J. Power Sources*, Vol. 161, pp. 1341-1345 (2006).
4. Thapa, A.K. et. al, "Novel graphite/TiO_2 electrochemical cells as a safe electric energy storage system," *Electrochem. Acta*, Vol. 55, pp. 7305-7309 (2010).
5. Zhang, S.S., "A new approach toward improved low temperature performance of Li-ion batteries," *Electrochem. Comm.*, Vol. 4, pp. 928-932 (2002).
6. Inui, Y., Kobayashi, Y., Watanabe, Y., Watase, Y., Kitamura, Y., "Simulation of temperature distribution in cylindrical and prismatic lithium ion secondary batteries," *Energy Conversion and Management*, Vol. 48, pp. 2103-2109 (2007).
7. Al-Hallaj, S. and Selman, J.R., "Thermal modeling of secondary lithium batteries for electric vehicle/hybrid electric vehicle applications," *J. Power Sources*, Vol. 110, pp. 341-348 (2002).
8. Kim, G.-H., Pesaran, A., and Spotnitz, R., "A three-dimensional thermal abuse model for lithium-ion cells," *J. Power Sources*, Vol. 170, pp. 476-489 (2007).
9. Botte, G.G., Subramanian, V.R., and White, R.E., "Mathematical modeling of secondary lithium batteries," *Electrochem. Acta*, Vol. 45, pp. 2595-2609 (2000).
10. Bandhauer, T.M., Garimella, S., and Fuller, T.F., "A critical review of thermal issues in lithium-ion batteries," *J. Electrochem. Soc.*, pp. R1-R25 (2011).
11. Pals, C.R. and Newman, J., "Thermal modeling of the lithium/polymer battery: II. Temperature profiles in a cell stack," *J. Electrochem. Soc.*, Vol. 142, pp. 3282-3288 (1995).
12. Chen, Y. and Evans, J. W., "Heat transfer phenomena in Lithium/ Polymer-electrolyte batteries for electric vehicle application," *J. Electrochem. Soc.*, Vol. 140, pp. 1833-1838 (1993).
13. Song, L. and Evans, J.W., "The thermal stability of lithium polymer batteries," *J. Electrochem. Soc.*, Vol. 145, pp. 2327-2334 (1998).
14. Kim, U.S., Shin, C.B., and Kim, C.-S., "Modeling for the scale-up of a lithium-ion polymer battery," *J. Power Sources*, Vol. 189, pp. 841-846 (2009).
15. Lee, J., Choi, K.W., Yao, N.P., and Christianson, C.C., "Three-dimensional thermal modeling of electric vehicle batteries," *J. Electrochem. Soc.*, Vol. 133, pp. 1286-1291 (1986).
16. Chen, Y. and Evans, J.W., "Three-dimensional thermal modeling of lithium-polymer batteries under galvanostatic discharge and dynamic power profile," *J. Electrochem. Soc.*, Vol. 141, pp. 2947-2955 (1994).
17. Chen, Y. and Evans, J.W., "Thermal analysis of lithium-ion batteries," *J. Electrochem. Soc.*, Vol. 143, pp. 2708-2712 (1996).
18. Chen, S.C., Wan, C.C., and Wang, Y.Y., "Thermal analysis of lithium-ion batteries," *J. Power Sources*, Vol. 140, pp. 111-124 (2005).
19. Newman, J. and Tiedemann, W., "Temperature rise in a battery module with constant heat generation," *J. Electrochem. Soc.*, Vol. 142, pp. 1054-1057 (1995).
20. Özişik, M.N., *Heat conduction*, 2nd ed., John Wiley & Sons, New York (1993).
21. Carslaw, H.S. and Jaeger, J.C., *Conduction of heat in solids*, 2nd ed., Clarendon Press, Oxford (1959).
22. Cooper, H.F., "Transient and steady-state temperature distribution in foil-wound solenoids and other electric apparatus of rectangular cross section," *IEEE Transaction on parts, materials and packaging*, Vol. 2, pp. 3-9 (1966).
23. Bernardi, D., Pawlikowski, E., and Newman, J., "A general energy balance for battery systems," *J. Electrochem. Soc.*, Vol. 132, pp. 5-12 (1985).
24. Rao, L. and Newman, J., "Heat-generation rate and general energy balance for insertion battery systems," *J. Electrochem. Soc.*, Vol. 144, pp. 2697-2704 (1997).
25. Yurkovich, B.J., Yurkovich, S., Guezennec, Y., and Hu, Y., "Electro-thermal battery modeling and identification for automotive applications," *Proceedings of the 2010 DSCC Conference*, 2010.
26. Sabbah, R., Kizilel, R., Selman, J.R., and Al-Hallaj, S., "Active (air-cooled) vs. passive (phase change material) thermal management of high power lithium-ion packs: Limitation of temperature rise and uniformity of temperature distribution," *J. Power Sources*, Vol. 182, pp. 630-638 (2008).
27. Incropera, F.P., DeWitt, D.P., Bergman, T.L., and Lavine, A.S., *Fundamentals of heat and mass transfer*, 6th ed., John Wiley & Sons., New York (2007).

DEFINITIONS/ABBREVIATIONS

A
total surface area of the battery

A_{ij}
area of battery individual surfaces (m^2)

Bi*$_{ij}$*
Biot numbers at battery individual surfaces

Bi*$_{Ave}$*
surface-averaged Biot number

c_p
heat capacity (J·kg^{-1}·K^{-1})

g
volumetric heat generation rate (W·m^{-3})

G
source of temperature rise (K)

$\bar{G}$
transformed source of temperature rise (K)
h_{ij}
convective heat transfer coefficients at battery surfaces ($W \cdot m^{-2} \cdot k^{-1}$)
I
battery current (A)
k_i
effective thermal conductivity in x_i-direction ($W \cdot m^{-1} \cdot K^{-1}$)
K_i
dimensionless effective thermal conductivity in x_i-direction
ℓ
thickness of battery layers in x_1-direction (m)
L_i
battery dimension in x_i-direction (m)
N
number of layers (components) in the battery core
t
time (s)
T
temperature (K)
T_0
ambient and initial temperatures (K)
V
battery voltage (V)
V_{oc}
open circuit potential (V)
$\mathcal{V}$
volume (m^3)
x_i
position in Cartesian coordinate system (m)
X_i
dimensionless position in Cartesian coordinate
η_i
normalization factor in X_i-direction
θ
temperature rise (K)
θ_{Ave}
average temperature rise (K)
θ_{Max}
maximum temperature rise (K)
θ_{Min}
minimum temperature rise (K)
$\bar{\theta}$
transformed temperature rise (K)
λ_i
list of eigenvalues in X_i-direction
ρ
mass density ($kg \cdot m^{-3}$)
τ
dimensionless time
ψ
transformation kernel
ϕ
eigenfunction

ICE
internal combustion engine
BTMS
battery thermal management system
DOD
depth-of-discharge
H/PEV
hybrid and plug-in electric vehicle
Li-ion
lithium-ion
OCP
open circuit potential
SOC
state-of-charge

APPENDIX

The integral transform technique for solving three-dimensional heat conduction equation in finite orthotropic regions with transient heat source/sink is presented below. More detailed discussion about the method is available in Ref. [20].

After transformation of the original system (1), (2), (3) to system (4), (5), (6), the triple integral transformation and inversion formula for temperature function θ (X_1, X_2, X_3,τ) are defined as

$$\overline{\theta}(\lambda_{1l},\lambda_{2m},\lambda_{3n},\tau)=\int_{X_1=0}^{1}\int_{X_2=0}^{1}\int_{X_3=0}^{1}\psi(\lambda_{1l},X_1')\cdot\psi(\lambda_{2m},X_2')\cdot\psi(\lambda_{3n},X_3')\cdot\theta(X_1',X_2',X_3',\tau)\cdot\mathrm{d}X_3'\cdot\mathrm{d}X_2'\cdot\mathrm{d}X_1' \tag{A-1}$$

$$\theta(X_1,X_2,X_3,\tau)=\sum_{l=1}^{\infty}\sum_{m=1}^{\infty}\sum_{n=1}^{\infty}\psi(\lambda_{1l},X_1)\cdot\psi(\lambda_{2m},X_2)\cdot\psi(\lambda_{3n},X_3)\cdot\overline{\theta}(\lambda_{1l},\lambda_{2m},\lambda_{3n},\tau) \tag{A-2}$$

The functions ψ (λ_{1l}, X_1), ψ (λ_{2m},X_2), and ψ (λ_{3n},X_3) are the transformation kernels (normalized eigenfunctions) for X_1-, X_2-, and X_3-directions,

$$\psi(\lambda_i,X_i)=\frac{\phi(\lambda_i,X_i)}{\eta_i^{1/2}}\ (i=1,2,3) \tag{A-3}$$

and $\phi(\lambda_i,X_i)$ are eigenfunctions of the Sturm-Loiuville system corresponding to Eqs. (4) and (5),

$$\frac{\mathrm{d}\phi}{\mathrm{d}X_i}+\lambda_i^2\phi=0 \tag{A-4-1}$$

$$-\frac{\mathrm{d}\phi}{\mathrm{d}X_i}+\mathrm{Bi}_{i0}\phi=0 \quad \text{at} \quad X_i=0\ (i=1,2,3) \tag{A-4-2}$$

$$\frac{\mathrm{d}\phi}{\mathrm{d}X_i}+\mathrm{Bi}_{i1}\phi=0 \quad \text{at} \quad X_i=1\ (i=1,2,3) \tag{A-4-3}$$

Series of eigenvalues in X_i-direction, λ_i, are obtained as positive roots of the following transcendental equation

$$\tan\lambda_i=\frac{\lambda_i\left(\mathrm{Bi}_{i0}+\mathrm{Bi}_{i1}\right)}{\lambda_i^2-\mathrm{Bi}_{i0}\mathrm{Bi}_{i1}}\ (i=1,2,3) \tag{A-5}$$

In (A-1) and (A-2), the subscripts l, m, and n represent the indices for eigenvalues in X_1-, X_2-, and X_3-direction, respectively.

The normalization factor η_i in (A-3) is

$$\eta_i=\frac{1}{2}\left[\left(\lambda_i^2+\mathrm{Bi}_{i0}^2\right)\left(1+\frac{\mathrm{Bi}_{i1}}{\lambda_i^2+\mathrm{Bi}_{i1}^2}\right)+\mathrm{Bi}_{i0}\right]\ (i=1,2,3) \tag{A-6}$$

The integral transform of Eq. (4), according to transformation (A-1), yields an ordinary differential equation,

$$\frac{\mathrm{d}\overline{\theta}}{\mathrm{d}\tau} + \Delta_{lmn}\overline{\theta} = \overline{G} \quad \text{with} \quad \overline{\theta}(\tau) = 0 \quad \text{at} \quad \tau = 0 \tag{A-7}$$

in which

$$\Delta_{lmn} = \lambda_{1l}^2 + K_2\lambda_{2m}^2 + K_3\lambda_{3n}^2 \tag{A-8}$$

Quantities with a bar refer to the integral transform as given by (A-1).
The solution for (A-7) reads

$$\overline{\theta}(\tau) = \frac{\overline{G}}{\Delta_{lmn}}\left(1 - \exp\left(-\Delta_{lmn}\tau\right)\right) \tag{A-9}$$

and replacing $\overline{\theta}(\tau)$ from the above solution into the inversion formula (A-2) gives the final solution in series form

$$\theta(X_1, X_2, X_3, \tau) = \sum_{l=1}^{\infty}\sum_{m=1}^{\infty}\sum_{n=1}^{\infty}\psi(\lambda_{1l}, X_1)\cdot\psi(\lambda_{2m}, X_2)\cdot\psi(\lambda_{3n}, X_3)\cdot\frac{\overline{G}}{\Delta_{lmn}}\left(1 - \exp\left(-\Delta_{lmn}\tau\right)\right) \tag{A-10}$$

in which

$$\overline{G}(\lambda_{1l}, \lambda_{2m}, \lambda_{3n}, \tau) = \int_{X_1=0}^{1}\int_{X_2=0}^{1}\int_{X_3=0}^{1}\psi(\lambda_{1l}, X_1')\cdot\psi(\lambda_{2m}, X_2')\cdot\psi(\lambda_{3n}, X_3')\cdot G(X_1', X_2', X_3', \tau)\cdot\mathrm{d}X_3'\cdot\mathrm{d}X_2'\cdot\mathrm{d}X_1' \tag{A-11}$$